Decadal Oceanic Response to Stochastic Wind Forcing

PAOLA CESSI

Scripps Institution of Oceanography, University of California, San Diego, La Jolla, California

STÉPHANIE LOUAZEL

SHOM/CMO, Brest, France

(Manuscript received 19 September 2000, in final form 15 March 2001)

ABSTRACT

The low-frequency linear eigenmodes of the reduced-gravity shallow-water equations with weak friction are calculated numerically and using an analytic approximation. For basins with a large variation of the Coriolis parameter, large-scale eigenmodes emerge: the eigenfrequencies are integer multiples of the frequency for the gravest mode, which, in turn, has a period given by the transit time of the slowest long Rossby wave. The *e*-folding decay times are comparable to the period and independent of friction. These eigenmodes are excited by stochastic wind forcing and this leads to a weak peak in the spectral response near the frequency of the least-damped eigenmode. This decadal-frequency peak is most evident on the eastern and western boundaries and in the equatorial region of the basin.

1. Introduction

Evidence of midlatitude decadal variability in the upper North Atlantic (Kushnir 1994), and in the North Pacific (Miller et al. 1998; Deser et al. 1999) has recently emerged. Because the oceanic circulation above the thermocline is primarily wind-driven, a simple explanation of this low-frequency variability is that the ocean responds linearly and passively to random atmospheric wind forcing (Frankignoul 1979). How then does the ocean dynamics filter stochastic atmospheric forcing? Frankignoul et al. (1997) consider the response of linear, planetary geostrophic dynamics to random wind-stress-curl forcing using an idealized geometry, namely, a semi-infinite basin, bounded to the east by a solid boundary coincident with a meridian. In this geometry the Rossby waves generated at the eastern boundary radiate westward without selecting any preferred timescale of response. Thus, in the model of Frankignoul et al. (1997) there are no oceanic resonances excited by atmospheric forcing. Moreover, the dependence on latitude of the spectrum is parametric. That is, the spectrum at one latitude can be obtained by scaling transformations of the spectrum at any other latitude.

However, the analysis of model data by Capotondi and Alexander (2001, hereafter CA) shows that, at least in the Tropics, the variability is concentrated at decadal timescales even if the wind forcing has a white spectrum. The variability is characterized by signals propagating westward at the local speed of long baroclinic Rossby waves. The timescale of the observed response is longer than the local transit time across the basin of long Rossby waves: the response has the timescale of Rossby waves in the middle latitudes.

In a closed basin, the quasigeostrophic analysis of Cessi and Primeau (2001) has shown that weakly dissipated basin modes can be resonantly excited at decadal frequencies. The existence of free-basin modes suggests the possibility of spectral peaks, associated with basinwide resonances, and nontrivial spatial response patterns.

The constraint of mass conservation is essential for the existence of low frequency, large-scale basin modes described by Cessi and Primeau (2001). In the context of quasigeostrophy, the mass conservation constraint is fulfilled by adjusting the boundary pressure, which is independent of position, but is time dependent (McWilliams 1977). The unsteady boundary pressure is the source of Rossby waves that propagate westward into the interior. In other words, the mass conservation constraint changes the linear response everywhere in the basin, by producing coupling between different latitudes and disparate scales (Cessi and Primeau 2001). This coupling is not included in the analysis of Frankignoul et al. (1997), and one of our goals here is to show how the mass conservation constraint alters the linear response to random wind forcing.

In the following we examine the linear, shallow-water

Corresponding author address: Paola Cessi, UCSD-0213, La Jolla, CA 92093-0213.
E-mail: pcessi@ucsd.edu

modes of a reduced-gravity layer forced by wind stress and dissipated by Rayleigh drag, in a closed domain of simple geometry. Unlike Cessi and Primeau (2001), the shallow-water formulation allows the full variation with latitude of the long Rossby wave speed. Thus the transit time of long Rossby waves varies from a few months near the equator to decades at the northern boundary of the domain. This strong variation in transit time has remarkable consequences: the damping rate of the modes does not depend on dissipation, as long as the latter is small. We find that, in the limit of weak dissipation, the real and imaginary parts of the eigenfrequencies can have comparable magnitudes and that the gravest, least dissipated mode has a decadal period.

2. The model

We consider a rectangular basin with $0 < y < L_y$ as the latitudinal coordinate and $0 < x < L_x$ as the longitudinal one. Our point of departure is the linear, reduced-gravity shallow-water equations, with friction and wind forcing. Assuming that friction is in the form of linear damping, the oceanic flow is governed by the momentum equations

$$u_t - fv = -g'h_x + \frac{\tau(y, t)}{\rho H} - ru, \tag{1}$$

$$v_t + fu = -g'h_y - rv, \tag{2}$$

and the mass conservation equation

$$h_t + H(u_x + v_y) = 0. \tag{3}$$

In (1)–(3):

- $f = f_0 + \beta_y$ is the Coriolis parameter;
- u and v are the zonal and meridional speed, respectively;
- r is the coefficient of linear drag;
- g' is the reduced gravity;
- ρ is the mean density;
- h is the displacement of the upper-layer depth around the constant value H; and
- τ is the zonal wind stress and is assumed to depend on y and t only.

Boundary conditions of no normal flow are imposed on the solid walls, that is, $\mathbf{u} \cdot \mathbf{n} = 0$, so that total mass is conserved:

$$\int_0^{L_x} \int_0^{L_y} h \, dy \, dx = 0. \tag{4}$$

The above integral constraint is obtained by integrating the mass conservation equation (3) over the domain and defining the mean layer thickness H as the initial average depth of the layer.

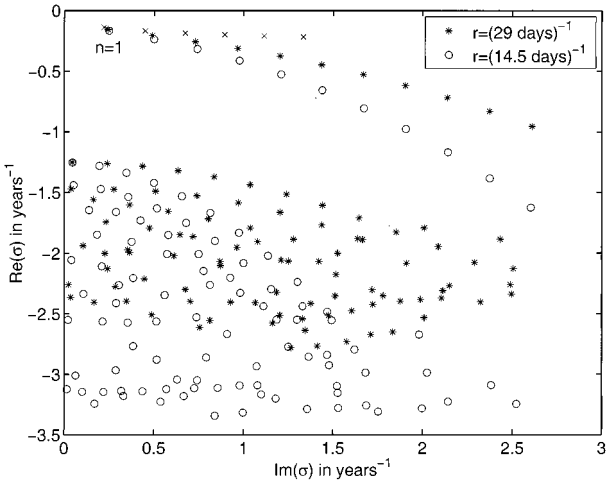

FIG. 1. Scatterplot of the low-frequency eigenvalues, σ, obtained by solving numerically (6) for two values of the friction, r (the decay rate is on the ordinate and the frequency on the abscissa). Also shown ($\times$) are the corresponding eigenvalues obtained using the approximate dispersion relation (16) that results from the interior eigenproblem in the inviscid, planetary geostrophic limit.

a. The eigenproblem

The time-dependent response of the linear system (1)–(3) depends both on the temporal and spatial structure of the forcing and on the intrinsic modes of variability of the unforced system. The latter can be obtained by solving the eigenproblem associated with the system. In other words, we assume that the solutions of the unforced reduced-gravity shallow-water equations have the form

$$\begin{pmatrix} h \\ u \\ v \end{pmatrix} = e^{\sigma t} \begin{pmatrix} \hat{h} \\ \hat{u} \\ \hat{v} \end{pmatrix} (x, y), \tag{5}$$

which gives

$$\sigma \begin{pmatrix} \hat{h} \\ \hat{u} \\ \hat{v} \end{pmatrix} = \mathcal{L} \begin{pmatrix} \hat{h} \\ \hat{u} \\ \hat{v} \end{pmatrix}: \tag{6}$$

σ are the eigenvalues of the matrix, $\mathcal{L}$, that results from the shallow-water equations plus the no-normal-flow boundary conditions, and is given by

$$\mathcal{L} = \begin{pmatrix} 0 & -H\partial_x & -H\partial_y \\ -g'\partial_x & -r & f \\ -g'\partial_y & -f & -r \end{pmatrix}. \tag{7}$$

The eigenvalues, σ, and the eigenvectors, $(\hat{h}, \hat{u}, \hat{v})$, are determined numerically by approximating $\mathcal{L}$ with a finite-difference C grid.

Figure 1 shows the low-frequency portion of the eigenspectrum obtained by solving (6) numerically (stars and circles) for two values of the frictional parameter

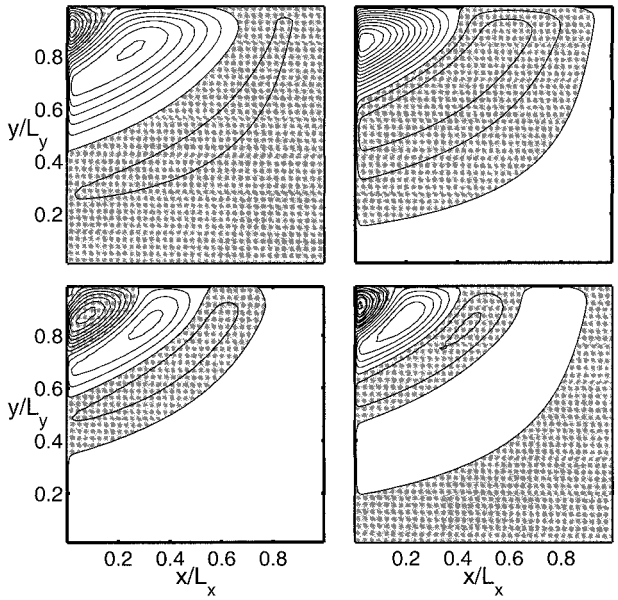

FIG. 2. (left) Real and (right) imaginary parts of the eigenfunctions, $\hat{h}$, associated with the (top) smallest and (bottom) next-to-smallest eigenvalues of Fig. 1 for $r = 8 \times 10^{-7}$ s^{-1} (14.5 days)$^{-1}$. (top) For mode 1 the eigenvalue is $\sigma = -0.1658 + i0.2504$ in yr^{-1}, corresponding to a period of 25.1 yr. (bottom) For mode 2 the eigenvalue is $\sigma = -0.2366 + i0.4998$ in yr^{-1}, corresponding to a period of 12.6 yr. Negative contours are shaded.

r. For this and subsequent calculations we use the following values:

$$f_0 = 2 \times 10^{-5}\ \text{s}^{-1}, \qquad \beta = 1.6 \times 10^{-11}\ \text{m}^{-1}\ \text{s}^{-1},$$
$$L_x = L_y = 7.5 \times 10^6\ \text{m}, \qquad H = 500\ \text{m},$$
$$g' = 0.02\ \text{m s}^{-2}. \tag{8}$$

A band of weakly damped eigenvalues emerges, the decay rate of which is much smaller than r. Moreover, the eigenvalues for the gravest modes in this band are independent of friction to leading order.

The eigenfunctions for $\hat{h}$ are shown in Fig. 2 for the two least damped eigenvalues. These modes are characterized by a large-scale interior spatial structure, with phase lines oriented southwest to northeast. A thin return flow is present along the western boundary, with a boundary layer width proportional to r.

b. The geostrophic, inviscid limit

Because the low-frequency eigenvalues in Fig. 1 are almost independent of friction, and the corresponding eigenfunctions have a large-scale structure away from a thin region near the western boundary, we can neglect both friction and inertia. This reduces the homogeneous, reduced-gravity momentum equations (1) and (2) to the statement of geostrophic balance, that is,

$$-fv = -g'h_x; \qquad fu = -g'h_y. \tag{9}$$

These diagnostic relations, together with the mass conservation equation (3), lead to the planetary geostrophic potential vorticity equation (PGPV):

$$h_t - ch_x = 0, \tag{10}$$

where $c(y) \equiv \beta g' H / f^2$ is the long Rossby wave velocity and is a strong function of latitude. Because the direction of propagation of c is westward, the single boundary condition allowed by (10) is $u = 0$ at $x = L_x$. This implies that h must be independent of latitude at the eastern boundary or

$$h = h_0(t) \quad \text{at} \quad x = L_x. \tag{11}$$

This boundary condition is insufficient to completely determine the layer depth. The boundary condition (11) must be supplemented by the constraint of total mass conservation (4). The application of the boundary condition (11) plus the constraint (4) will be justified in section 4 with an asymptotic analysis of the linear shallow-water equations valid for timescales longer than r^{-1} with $r \ll f$. The conclusions of section 4 are the following.

1) Friction affects the solution only in thin boundary layers, so that the mass conservation constraint can be applied to the interior inviscid solution in the limit of weak friction.
2) The boundary pressure, proportional to $h_0(t)$, cannot be specified as an arbitrary constant. Instead, the time evolution of $h_0(t)$ is determined by (48).

We now determine the eigenfunctions and eigenvalues, by looking for solutions to (10) of the form

$$h = e^{\sigma t}\hat{h}(x, y). \tag{12}$$

The eigenvalue is σ and $\hat{h}$ is the eigenfunction, which satisfies the boundary condition $\hat{h}(L_x, y) = \hat{h}_0$, and is subject to the constraint

$$\int_0^{L_x}\int_0^{L_y} \hat{h}\, dy\, dx = 0. \tag{13}$$

The solution of (10), which fulfills the eastern boundary condition is

$$h = \hat{h}_0 e^{\sigma[t + (x - L_x)/c]}. \tag{14}$$

Thus, the solution is a Rossby wave that propagates at the local long Rossby wave speed, c. The longitudinal wavelength of this wave is $c(y)/\sigma$ and, thus, decreases with latitude. The eigenvalues are determined by enforcing the mass conservation constraint (13). Evaluating the x integral in (13) gives

$$\int_0^{L_y} c(y)[e^{-\sigma L_x/c(y)} - 1]\, dy = 0, \tag{15}$$

which is a special case of (48) obtained for $\tau = 0$ and $h_0 = \hat{h}_0 e^{\sigma t}$. Next, using the definition of c and performing the y integral in (15) gives the transcendental dispersion relation

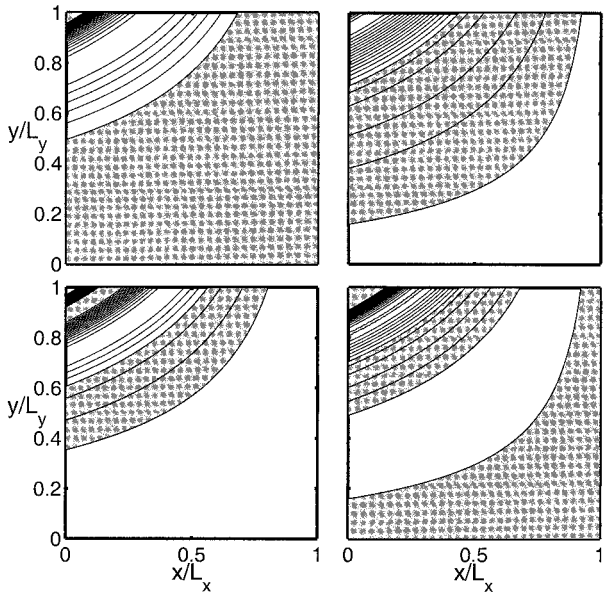

FIG. 3. (left) Real and (right) imaginary parts of the two gravest planetary geostrophic, inviscid eigenfunctions, $\hat{h}$, given by (14). (top) For the gravest mode the eigenvalue is $\sigma = -0.1377 + i0.2222$ in yr^{-1}. (bottom) For the next mode the eigenvalue is $\sigma = -0.1684 + i0.4504$ in yr^{-1}. The contour level is the same as that used in Fig. 2 and negative contours are shaded.

$$\frac{e^{-\sigma T_S(1+\alpha)^2} + \alpha}{1+\alpha} - e^{-\sigma T_S} + \sqrt{\sigma T_S \pi}\left\{\mathrm{erf}\left[\sqrt{\sigma T_S}(1+\alpha)\right] - \mathrm{erf}\left[\sqrt{\sigma T_S}\right]\right\} = 0, \tag{16}$$

where erf(z) is the error function, $\alpha \equiv \beta L_y / f_0$, and

$$T_S \equiv \frac{L_x}{c(0)} \tag{17}$$

is the basin transit time of Rossby waves at the southern boundary, $y = 0$. The dispersion relation equation is solved numerically. There is an infinitude of modes with eigenvalue σ_n, which depend on the parameter α. The gravest six eigenvalues for the parameter values in (8) (corresponding to $\alpha = 6$) are shown in Fig. 1 (crosses). There is good agreement between the interior PGPV approximation and the full inertial and frictional problem for the gravest mode, $n = 1$, and convergence, as $r \to 0$ is suggested for the higher modes. Moreover, the eigenfunctions (14), shown in Fig. 3, agree with the solutions of the shallow-water eigenproblem (cf. Figs. 2 and 3), except in the western and northern boundary layers.

Figure 4 shows the decay rates and the frequencies of the first two modes as a function of α. Notice that the frequency of the gravest mode, $n = 1$, is always less than $2\pi/T_S$, so that the period is always longer than the transit time at the southern boundary.

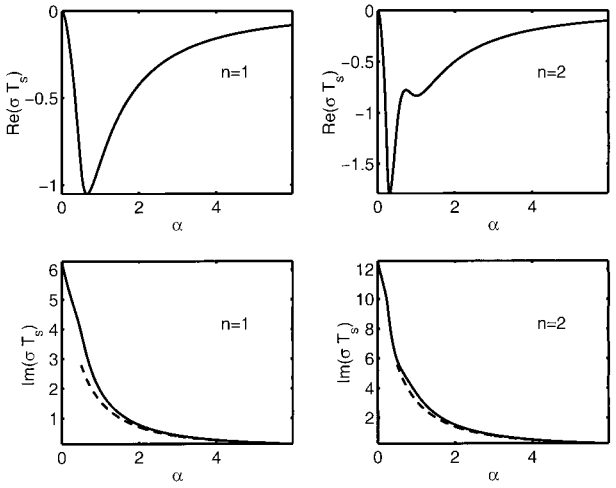

FIG. 4. (top) Normalized decay rates, Re(σT_S), and (bottom) frequencies, Im(σT_S), for the first two modes as a function of $\alpha \equiv \beta L_y / f_0$ (solid line). The dashed line in the lower panels is the approximation $\omega_n T_S \approx 2\pi n(1+\alpha)^{-2}$ valid for large α.

Specifically, the behavior of the frequency for large α is approximately given by $\omega_n \approx 2\pi n T_S^{-1}(1+\alpha)^{-2}$ (dashed line in Fig. 4). Because of the equality $T_S(1+\alpha)^2 = L_x/c(L_y)$, the eigenperiod in the limit of large α approaches the transit time of the slowest Rossby wave. In other words, the eigenperiod is given by the transit time of the wave traveling along the northern boundary, $y = L_y$, even though the apparent speed of the phase lines equals the local long Rossby wave speed. These features also characterize the thermocline variability obtained by CA in an eddy-resolving ocean general circulation model.

Unless α is small the decay rate is of the same magnitude as the frequency. For small α, σ can be determined from (16) as an expansion in powers of α, and we find

$$\sigma T_S = 2\pi i n(1 - \alpha + \alpha^2) - \frac{2}{3}(\alpha\pi n)^2 + O(\alpha^3). \tag{18}$$

The quasigeostrophic limit is recovered in the limit $\alpha \to 0$, and in this case the eigenvalue predicted by the inviscid limit is purely imaginary, in accord with the results of Cessi and Primeau (2001).

For finite α, the eigenvalues, σ_n, of the inviscid PGPV problem have a negative real part. Remarkably, this means that for small friction, $r \ll f$, the damping rate Re(σ) is, to leading order, independent of the friction r and can be determined without having to resolve the details of the frictional boundary layers on the northern, western, and southern boundaries necessary to close the circulation. Inspection of the eigensolutions (14) reveals that, except in the quasigeostrophic limit, the phase lines at the western wall are tilted, so that the component of the flow into the boundary is returned in a viscous layer, where some of the energy is dissipated. In this respect the planetary geostrophic equations differ crucially from

the quasigeostrophic limit examined by Cessi and Primeau (2001), where the interior phase lines are parallel to the boundary, and no dissipation occurs to leading order.

In summary, the reduced-gravity shallow-water equations possess a set of low-frequency, weakly damped, decadal basin modes. Because these modes are large scale and not influenced by friction, they are accurately described by the interior planetary geostrophic dynamics and mass conservation.

3. Stochastic forcing

In this section we examine the response to a wind stress that is stochastic in time. The goal is to determine whether the existence of damped, large-scale modes leads to a preferred timescale of response. Thus, we examine the solution of the stochastically forced, inviscid planetary geostrophy formulation (10)

$$h_t - ch_x = \left(\frac{\tau}{f\rho}\right)_y, \tag{19}$$

subject to (4) and (11). A detailed derivation of this approximation from the shallow-water equations is given in section 4.

Following Frankignoul et al. (1997), we consider a wind forcing:

$$\tau(y, t) = \tau_0 w(t) g(y), \tag{20}$$

where $g(y)$ is the spatial shape of the forcing and $w(t)$ is a random number, picked at every time step from a Gaussian distribution, with zero average and a power spectrum with unit amplitude.

Solutions are readily obtained by taking the Fourier transform of (19), that is,

$$\begin{aligned} i\omega\hat{h} - c\hat{h}_x &= \hat{w}\tilde{g}, \\ \hat{h}(L_x, y, \omega) &= \hat{h}_0(\omega), \\ \int_0^{L_x} dx \int_0^{L_y} \hat{h}\, dy &= 0. \end{aligned} \tag{21}$$

Here we have defined $\tilde{g} \equiv [\tau_0 g/(\rho f)]_y$, and the hat indicates the Fourier transform. The solution of (21) is

$$\hat{h} = -i\omega^{-1}\hat{w}\tilde{g} + (\hat{h}_0 + i\omega^{-1}\hat{w}\tilde{g})e^{i\omega(x-L_x)/c}, \tag{22}$$

where $\hat{h}_0$ is the Fourier transform of the depth at the eastern boundary. The mass constraint determines $\hat{h}_0$ to be

$$\hat{h}_0(\omega) = \hat{w}\left[\int_0^{L_y} c(y)(e^{-i\omega L_x/c(y)} - 1)\, dy\right]^{-1} \times \int_0^{L_y} \tilde{g}(y)[L_x - i\omega^{-1}c(y)(e^{-i\omega L_x/c(y)} - 1)]\, dy, \tag{23}$$

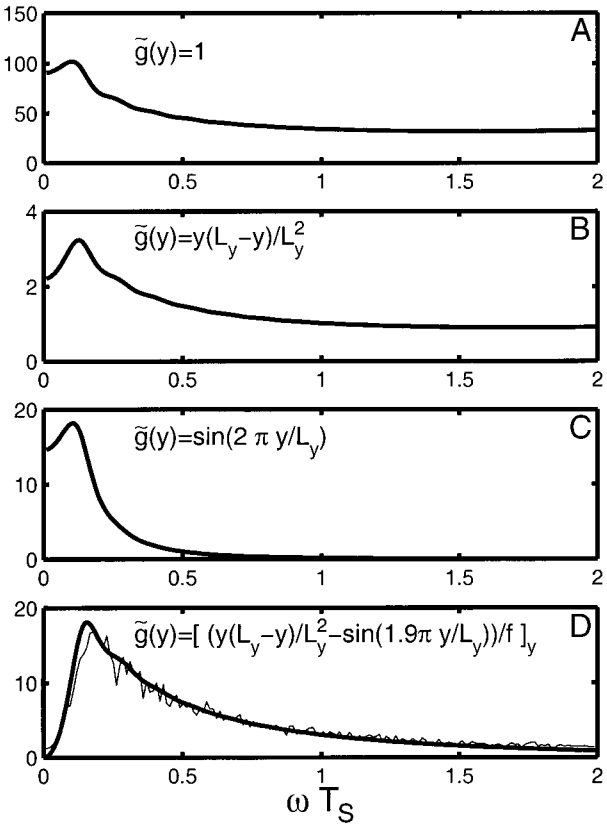

FIG. 5. Power spectrum of $h_0(t)$ for four different shapes $\tilde{g}(y)$. The spectral peaks are located at (a) $\omega T_S = 0.10$, (b) 0.13, (c) 0.11, and (d) 0.16. In (d) the power spectrum obtained by averaging 100 realizations of the numerical solutions of (25) for $r = 4 \times 10^{-7}$ s^{-1} is also shown (thin line), illustrating the good agreement with the interior analytic approximation (thick line).

which is a special case of (48). The spectrum is obtained by forming the square of the absolute value of (22), and ensemble averaging with $\langle|\hat{w}|^2\rangle = 1$. Because all the eigenvalues are complex the denominator in (23) does not have a zero for ω real.

In Fig. 5 we plot the power spectrum at the eastern boundary, $\langle|\hat{h}_0|^2\rangle$, with $\hat{h}_0$ given by (23), for the following shapes of the forcing:

1) $\tilde{g}(y) = 1$,
2) $\tilde{g}(y) = y(L_y - y)/L_y^2$,
3) $\tilde{g}(y) = \sin(2\pi y/L_y)$,
4) $\tilde{g}(y) = [(y(L_y - y)/L_y^2 - \sin(1.9\pi y/L_y))/f]_y$.

In all cases the parameters have the values given in (8), and all of the spectra have a peak at low frequencies.[1] For the shape 4 we also performed computations using the planetary geostrophic equation (25) with $r = 4 \times 10^{-7}$ s^{-1}. The spectrum in this case is obtained by av-

[1] In this linear formulation the amplitude of the response is directly proportional to the amplitude of $\tilde{g}$, which is set to a number of order unity in all cases.

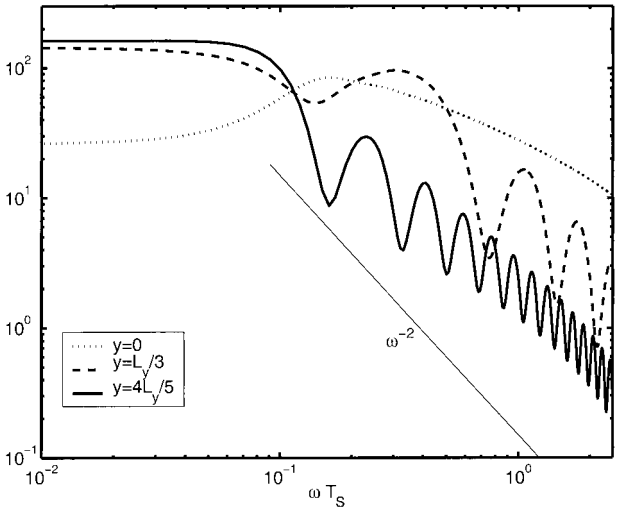

FIG. 6. Power spectrum of h at the outer edge of the western boundary for different latitudes. The forcing is $\tilde{g} = \{[y(L_y - y)/L_y^2 - \sin(1.9\pi y/L_y)]/f\}_y$.

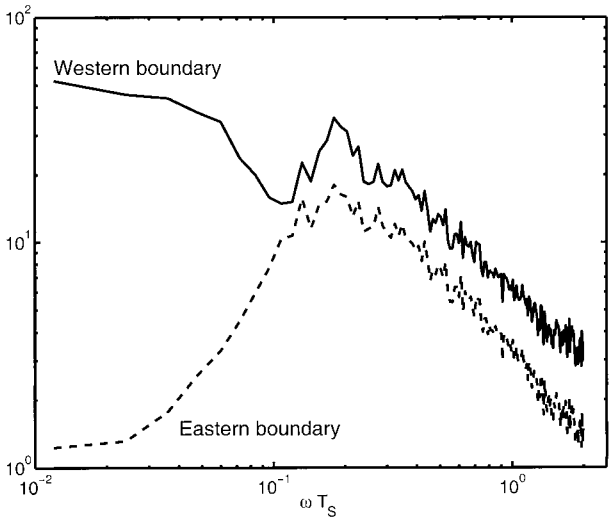

FIG. 7. Power spectrum of h at $y = 4/5L_y$ on the western boundary (solid line) and on the eastern boundary (dashed line), obtained by averaging 90 realizations of the numerical solutions of (25), for $r = 4 \times 10^{-7}$ s^{-1}. The forcing and parameters are the same as in Fig. 6.

eraging 100 realizations of the solutions of (25), each 312 yr long (the time step is 0.0012 yr). There is a close correspondence between the spectrum obtained with and without friction, although in the latter case the spectral peak occurs at a slightly lower frequency, as expected from the comparison shown in Fig. 1. Figure 5 illustrates that a preferred decadal timescale emerges regardless of the shape of the forcing. Specifically, expression (23) shows that $\hat{h}_0(\omega)$ does not vanish when the average of $\tilde{g}(y)$ is zero, in contrast to the quasigeostrophic limit of Cessi and Primeau (2001). As suggested by the analysis of the damped harmonic oscillator, the maximum of the forced response does not occur at the real part of the eigenfrequency. Moreover, different spatial wind stress configurations have different efficiencies in the excitation of the free modes, so that the position of the spectral maximum depends weakly on the wind pattern. But, despite these details, in all cases a low-frequency spectral peak is produced by the random forcing.

Away from the eastern boundary, the spectrum has a complicated spatial dependence. This is in contrast with the results of Frankignoul et al. (1997), where the spectrum has the same shape everywhere. As an illustration, we show in Fig. 6 the spectrum of h at the seaward edge of western boundary for $\tilde{g}$ in (iv) for different values of y. The spectrum is obtained by evaluating the interior approximation (22) at $x = 0$. The peak at decadal frequency found on the eastern boundary is also present on the western side of the basin only near the equator. However, as higher latitudes are reached, the peak migrates to zero frequency, and approaches the spectrum calculated by Frankignoul et al. (1997).

The interior approximation (22) is not valid in the frictionally controlled western boundary layer. In order to calculate the spectrum on the western wall we integrated numerically the planetary geostrophic equation (25) subject to the no-normal-flow conditions on the four solid boundaries. The wind stress is the same as that used for Fig. 6 and $r = 4 \times 10^{-7}$ s^{-1}. Ninety realizations, each 312 yr long, were averaged to obtain the spectrum shown in Fig. 7. Although we only show one latitude, $y = 4L_y/5$, this is representative of the whole spectrum at the western boundary. The spectral peak obtained on the eastern boundary (dashed line) is clearly discernible on the western boundary as well (solid line), above the directly forced low-frequency spectrum. The emergence of a peak associated with the least damped eigenmode on the western boundary should be contrasted with the prediction from the interior approximation: the spectrum at the seaward side of the western boundary current at the same latitude, shown as solid line in Fig. 6, has a minimum in the frequency band where the boundary spectra have a maximum. This result reinforces the importance of the time-varying boundary pressure in the excitation of the low-frequency basin modes.

Thus, different frequencies dominate the response to stochastic forcing in different parts of the basin. Although the details of the spectrum shape vary with the distribution of forcing, the decadal spectral peak due to the excitation of the basin modes dominates on the boundaries and in the equatorial region. The zero-frequency saturation discussed in Frankignoul et al. (1997) applies on the seaward side of the western boundary layer.

4. The boundary layers

In this section we provide a detailed analysis to justify the application of the constraint (4) as a supplement to

the eastern boundary condition (11) in the large-scale, low-frequency, weakly damped limit.

For timescales much longer than a day the acceleration terms are negligible compared with the Coriolis term in the shallow-water momentum equations, so that

$$-fv = -g'h_x + \frac{\tau(y, t)}{\rho H} - ru;$$
$$fu = -g'h_y - rv. \tag{24}$$

Combining the planetary geostrophic equations (24) with mass conservation (3), a single evolution equation for h is obtained:

$$h_t - \beta g'H\frac{f^2 - r^2}{(f^2 + r^2)^2}h_x = rg'H\nabla\left(\frac{\nabla h}{r^2 + f^2}\right) + \frac{1}{\rho}\left(\frac{f\tau}{r^2 + f^2}\right)_y, \tag{25}$$

with u and v related diagnostically to h by

$$(r^2 + f^2)u = -g'(rh_x + fh_y) + \frac{r\tau}{\rho H}, \tag{26}$$

$$(r^2 + f^2)v = g'(fh_x - rh_y) - \frac{f\tau}{\rho H}. \tag{27}$$

The requirement of no normal velocity gives the boundary conditions

$$-g'(rh_x + fh_y) + \frac{r\tau}{\rho H} = 0 \quad \text{at } x = 0 \quad \text{and} \quad \text{at } x = L_x, \tag{28}$$

$$g'(fh_x - rh_y) - \frac{f\tau}{\rho H} = 0 \quad \text{at } y = 0 \quad \text{and} \quad \text{at } y = L_y, \tag{29}$$

The evolution equation (25) with the boundary conditions (28) and (29) imply total mass conservation, that is,

$$\int_0^{L_x}\int_0^{L_y} h\, dy\, dx = 0. \tag{30}$$

In the following we will show that the enforcement of global mass conservation (30) determines the interior solution in the limit of small drag without becoming involved in the details of the frictional boundary layers.

a. The limit of small drag

In a closed domain the pressure on the eastern boundary cannot be arbitrarily set to zero as in Frankignoul et al. (1997). Instead, the boundary pressure is an unknown that must be determined as part of the solution by enforcing the no-normal-flow conditions and global mass conservation. However, in the planetary geostrophic formulation, the role of the eastern boundary pressure is not so obvious as in the quasigeostrophic case considered by McWilliams (1977). In the following we clarify this point.

In the limit where $r \ll f$, and away from the equator, (25) can be simplified as follows:

$$h_t - c(y)h_x = rg'H\nabla\left(\frac{\nabla h}{f^2}\right) + \left(\frac{\tau}{f\rho}\right)_y, \tag{31}$$

where $c(y) \equiv \beta g'H/f^2$ is the wave velocity. The first term on the right-hand side of (31) is negligble except in boundary layers.

b. Interior problem

The interior solution of (31), $h_I(x, y, t)$, satisfies

$$h_{It} - c(y)h_{Ix} = \left(\frac{\tau}{f\rho}\right)_y. \tag{32}$$

Because waves propagate westward, the eastern boundary does not support a viscous boundary layer, and we enforce the eastern boundary condition on the interior solution. Also, when applying (28) at $x = L_x$, we can neglect the terms proportional to r, so that to leading order in $r/f \ll 1$ we have

$$h_I = h_0(t) \quad \text{at} \quad x = L_x. \tag{33}$$

Applying this eastern boundary condition, the solution of (32) is

$$h_I(x, y, t) = h_0\left(t + \frac{x - L_x}{c(y)}\right) + \int_{t+(x-L_x)/c(y)}^{t}\left[\frac{\tau(y, t')}{f\rho}\right]_y dt'. \tag{34}$$

Because we anticipate that the corrections to the interior solution are confined to thin frictional boundary layers, we can apply the constraint of total mass conservation (4) to the interior solution, h_I. This requirement determines the eastern boundary depth, $h_0(t)$. Thus, we substitute (34) into

$$\int_0^{L_x}\int_0^{L_y} h_I\, dy\, dx = 0, \tag{35}$$

and obtain the integral equation that governs the evolution of $h_0(t)$:

$$\int_0^{L_y} c(y)\, dy \times \int_{t-T(y)}^{t}\left\{h_0(s) + [s - t + T(y)]\left[\frac{\tau(y, s)}{f\rho}\right]_y\right\} ds = 0, \tag{36}$$

where the transit time is $T(y) \equiv L_x/c(y)$. The eastern boundary depth $h_0(t)$ thus depends on the structure of the wind at all latitudes. For example, in the steady case where τ only depends on y, and where h_0 is a constant, we find

$$h_0 = -\frac{L_y^{-1}}{2}\int_0^{L_y}\left(\frac{\tau}{f\rho}\right)_y T\,dy. \tag{37}$$

Now we have to check that the heuristic argument leading to the approximation (35) is consistent with the existence of thin frictional boundary layers that allow the full application of the no-normal-flow conditions (28) and (29).

c. Boundary layers

In order to determine h on the northern, southern, and western boundaries, it is necessary to estimate the boundary layer widths.

1) Southern and northern boundary layers

The width of the meridional boundary layers is determined by a balance between βh_x and $-rh_{yy}$ in (31). This balance implies that the width of the southern (and northern) boundary layer is $O(\sqrt{rL_x/\beta})$. Thus, in (29), the frictional term, rh_y, is proportional to $\sqrt{r}$, and consequently rh_y is negligible compared to fh_x if $r \ll f$. Thus, the approximate boundary condition on the southern boundary is

$$h_x = \tau/(g'\rho H) + O(\sqrt{r\beta L_x}/f) \quad \text{at } y = 0. \tag{38}$$

Equation (38) can be integrated to give

$$h(x, 0, t) \approx (x - L_x)\tau/(g'\rho H) + h_0(t) \quad \text{at } y = 0. \tag{39}$$

Notice that, in the quasigeostrophic approximation, the southern boundary condition would be $h(x,0,t) = h_0(t)$. Thus, we expect $(x - L_x)\tau/(g'\rho H h_0) \ll 1$ in the quasigeostrophic limit. Equation (36) indicates that the order of magnitude of the variation of h_0 is $L_x\tau f(\beta L_y \rho g' H)^{-1}$, in accord with Sverdrup balance. With this estimate, the ratio of the first to the second term on the right-hand side of (39) is $O(\beta L_y/f)$, which is indeed small in the quasigeostrophic approximation. The treatment of the northern boundary follows that of the southern boundary. In summary, the boundary values of h are given by

$$\begin{aligned} h(x, L_y, t) &\approx (x - L_x)\tau_N/(g'\rho H) + h_0(t), \\ h(x, 0, t) &\approx (x - L_x)\tau_S/(g'\rho H) + h_0(t), \\ h(L_x, y, t) &\approx h_0(t), \end{aligned} \tag{40}$$

where τ_N and τ_S are the values of the wind stress at the northern and southern boundaries, respectively.

Figure 8 compares the approximate prediction (40) with the results of a numerical integration of the intertialess shallow-water equation (25). For this calculation we used the parameter values given in (8) and $r = 4 \times 10^{-7}\ \mathrm{s}^{-1}$. The wind stress is assumed periodic in time of the form

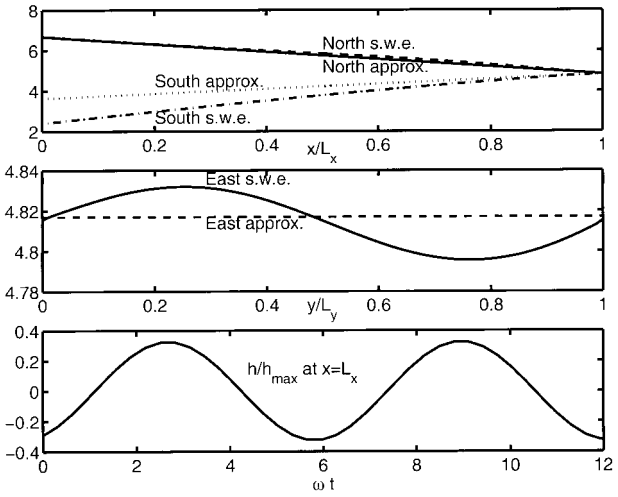

FIG. 8. The top two panels show snapshots of the depth of the layer, h, on the boundaries from the numerical solution of the shallow-water equations (s.w.e.) (25) and from the approximation in (40). The values on the northern and southern boundaries are on the top panel, while the values on the eastern boundary are in the middle panel. Notice the narrow range of values on the eastern boundary. The lower panel shows a time series of the layer's depth on the eastern boundary from the numerical solution, normalized by the maximum value obtained in the basin. The shape of the forcing is given in (41), and $\omega = 0.28\ \mathrm{yr}^{-1}$.

$$\tau = [L_y^{-2}(y - L_y/5)(y - L_y) + \sin(1.9\pi y/L_y)]\cos(\omega t). \tag{41}$$

The approximation (40) is very good on the eastern and northern boundaries, but less so on the southern boundary where the frictional parameter, $\sqrt{r\beta L_x}/f_0$, is not much less than unity. Also shown in Fig. 8 (bottom) is a time series of the boundary depth at the eastern boundary for the numerical solution of (25). The amplitude of the boundary depth has been normalized by the maximum value in the basin within an oscillation to emphasize that the variations in time of the boundary depth are substantial.

2) Western boundary

On the western wall we anticipate that friction will be important, and the width of the boundary layer is found by assuming a balance between βh_x and rh_{xx}. In this case the width of the western boundary layer is proportional to r and the western boundary condition is, to leading order in r/f,

$$rh_x + fh_y = 0 \quad \text{at} \quad x = 0. \tag{42}$$

Unlike the other three boundaries, we must retain the frictional term, and the determination of the western value of h, denoted by $h_1(y, t)$, requires the analysis of the western boundary layer. The solution within this region is the sum of the interior flow, h_I plus a western boundary layer correction, h_W. The interior flow is given by (34), and the correction satisfies

$$(rh_{Wx} + \beta h_W)_x = 0, \tag{43}$$

subject to the boundary conditions

$$h_I(0, y, t) + h_W(0, y, t) = h_1, \qquad \lim_{x\to\infty} h_W = 0. \tag{44}$$

From (43) and (44),

$$h_W(x, y, t) = \left\{ h_1(y, t) - h_0[t - T(y)] - \frac{1}{\rho}\int_{t-T(y)}^{t} \left[\frac{\tau(y, t')}{f}\right]_y dt' \right\} e^{-(\beta x/r)}. \tag{45}$$

To evaluate $h_1(y, t)$, the condition (42) is applied to $h_I + h_W$. To leading order in r, we obtain:

$$\left(\frac{h_1}{f}\right)_y = -\frac{\beta}{f^2}\left\{ h_0[t - T(y')] + \frac{1}{\rho}\int_{t-T(y)}^{t} \left[\frac{\tau(y, t')}{f}\right]_y dt' \right\}. \tag{46}$$

Thus, the variation of h_1 along the western boundary is $O(\beta L_y/f)$ and can be neglected in the quasigeostrophic limit. Therefore, in the quasigeostrophic approximation h is independent of the boundary arc length on all boundaries (McWilliams 1977).

In the shallow-water case, h_1 varies along the western boundary according to (46), which must be integrated subject to matching at $y = 0$, with the value on the southwest corner given by (39). Therefore,

$$\frac{h_1}{f} = \frac{h_0(t)}{f_0} - \frac{L_x\tau_S}{g'\rho H f_0} - \int_0^y \frac{\beta}{f^2}\left\{ h_0[t - T(y')] + \int_{t-T(y')}^{t} \left[\frac{\tau(y', t')}{f\rho}\right]_{y'} dt' \right\} dy'. \tag{47}$$

The continuity of h all around the rim of the basin requires h_1 to match the value on the northwest corner as given by (40), and this places the following constraint on h_0

$$\frac{h_0(t)}{f_N} - \frac{h_0(t)}{f_0} = \frac{L_x}{g'\rho H}\left[\frac{\tau_N}{f_N} - \frac{\tau_S}{f_0}\right] - \int_0^{L_y} \frac{\beta}{f^2}\left\{ h_0[t - T(y)] + \int_{t-T(y)}^{t} \left[\frac{\tau(y, t')}{f\rho}\right]_y dt' \right\} dy, \tag{48}$$

where f_N is the northerly value of f. This same constraint is obtained if the *interior* equation (32) is integrated over the domain, and the *interior* eastern boundary condition (33) and integral condition (35) are applied. Thus, the interior problem posed in section 3a, with the eastern boundary condition in (33) and the integral constraint (35), is a consistent approximation in the limit of small friction.

5. Conclusions

The weakly dissipated linear reduced-gravity shallow-water equations in a closed domain have been examined. The low-frequency eigenmodes of this system are characterized by large-scale oscillations with decadal periods. For a basin spanning a large latitudinal band, the period of the gravest mode is given by the transit time of the slowest long Rossby wave in the basin. The modes are characterized by long Rossby waves with phase speeds and wavenumbers that strongly vary with latitude. The basinwide coupling of these Rossby waves occurs on the eastern boundary, where the pressure signal is synchronized. The eastern boundary pressure rearranges the density field so as to fulfill the global constraint of mass conservation, and its time evolution is governed by (48).

In the limit of weak friction the damping rate of each eigenmode has a magnitude comparable to its frequency and, thus, approximately independent of friction. The damping arises because long Rossby waves are partially absorbed on the western boundary. The absorption is especially effective in basins of large latitudinal extent because the wavefronts are tilted by the differential phase speed. Since for Rossby waves the velocity is parallel to the wave crests, the more the waves are slanted in the east–west direction the more dissipation occurs in the western boundary layer. Indeed, the modal damping rate increases with the difference between the lowest and highest Rossby wave speeds.

Because the interior spatial structure of the eigenmodes is of large scale, their dynamics relies only on geostrophic balance and mass conservation. We thus anticipate that these findings are robust to changes in the details of the basin geometry. Specifically, given the high-latitude loading of the eigenmodes, the presence of a solid wall located in the proximity of the equator is of no consequence. To be sure, we repeated the eigenvalue calculation shown in Fig. 1 for a basin that straddles the equator symmetrically, and the low-frequency eigenvalues and eigenfunctions were almost unchanged.

The damped basin modes are excited by stochastic wind forcing, and the spectrum of the forced response exhibits a weak decadal peak on the eastern and western boundaries and in the equatorial region of the basin. Because of the wave properties of the oceanic response, the forced disturbances propagate at the local speed of long Rossby waves, as found by CA in an analysis of

an ocean general circulation model. We thus interpret the decadal peak found in CA as a basinwide, quasi-resonant response to wind forcing.

It is surprising that a decadal peak is more apparent near the equator, where the transit time of Rossby waves is fastest. However, all the latitudes are coupled by the pressure at the boundary, and the response at any given latitude depends on the global forcing as well as on the local one, with the latter dominating at higher latitudes. Thus, the excitation of basin modes is a mechanism by which midlatitudes exert control over the Tropics on decadal timescales.

As the western boundary is approached, the response depends on the time history of the wind forcing, from the time when the Rossby waves left the eastern boundary up to the present [cf. the expression for the interior depth (34)]. Thus, the interior response on the western side of the basin is dominated by ultra-low frequencies, which mask the decadal quasi-resonance. However, as the western wall is reached, the boundary pressure signal becomes prominent, and the spectral peak due to the least damped eigenmode emerges.

In this model the wind stress is prescribed as a random variable. However, several authors (Jin 1997; Munich et al. 1998) have suggested that the upper-ocean heat content (proportional to h in the present model), influences the wind itself. We conjecture that the basin modes, if coupled to the wind stress, can become sustained instead of damped, thus contributing to the decadal band of climate variability.

Acknowledgments. Funding for this research is provided by the National Science Foundation and the Department of Energy.

REFERENCES

Capotondi, A., and M. Alexander, 2001: Rossby waves in the tropical North Pacific and their role in decadal thermocline variability. *J. Phys. Oceanogr.*, in press.

Cessi, P., and F. Primeau, 2001: Dissipative selection of low-frequency modes in a reduced-gravity basin. *J. Phys. Oceanogr.,* **31,** 127–137.

Deser, C., M. Alexander, and M. Timlin, 1999: Evidence for a wind-driven intensification of the Kuroshio Current extension from the 1970s to the 1980s. *J. Climate,* **12,** 1697–1706.

Frankignoul, C., 1979: Stochastic forcing models of climate variability. *Dyn. Atmos. Oceans,* **3,** 465–479.

——, P. Müller, and E. Zorita, 1997: A simple model of the decadal response of the ocean to stochastic wind forcing. *J. Phys. Oceanogr.,* **27,** 1533–1546.

Jin, F., 1997: A theory of interdecadal climate variability of the North Pacific ocean–atmosphere system. *J. Climate,* **10,** 1821–1835.

Kushnir, Y., 1994: Interdecadal variations in North Atlantic sea surface temperature and associated atmospheric conditions. *J. Climate,* **7,** 141–157.

McWilliams, J., 1977: A note on a consistent quasigeostrophic model in a multiply connected domain. *Dyn. Atmos. Oceans,* **1,** 427–441.

Miller, A., D. Cayan, and W. White, 1998: A westward-intensified decadal change in the North Pacific thermocline and gyre-scale circulation. *J. Climate,* **11,** 3112–3127.

Munich, M., M. Latif, S. Venzke, and E. Maier-Reimer, 1998: Decadal oscillations in a simple coupled model. *J. Climate,* **11,** 3309–3319.